Preparation of spherical α-Fe$_2$O$_3$ nanoparticles and its photocatalytic degradation of MO and MB

Wenning Mu[a,b,c,d,*], Xueqing Xu[a,c,d], Haixia Xin[a,b,d], Tengfei Xiao[a,c,d], Xuefei Lei[a,b,d], Shaohua Luo[a,c,d]

[a]*School of Resources and Materials, Northeastern University at Qinhuangdao, Qinhuangdao 066004, Hebei, China,
emails: muwn@neuq.edu.cn (W. Mu), 1459559289@qq.com (X. Xu), 2365763078@qq.com (H. Xin), 2549598647@qq.com (T. Xiao),
danae2007@163.com (X. Lei), xinyue200@163.com (S. Luo)*
[b]*School of Metallurgy, Northeastern University, Shenyang 110819, Liaoning, China*
[c]*School of Materials Science and Engineering, Northeastern University, Shenyang 110819, Liaoning, China*
[d]*Key Laboratory of Resources Cleaner Conversion and Efficient Utilization Qinhuangdao City, Qinhuangdao 066004, Hebei, China*

ABSTRACT

A spherical α-Fe$_2$O$_3$ nano photocatalyst was successfully prepared via a simple process of chemical precipitation-calcination. The effects of solution end pH, ammonia concentration, and precursor calcination temperature on the morphology, structure, and properties of the as-prepared α-Fe$_2$O$_3$ particles were studied in detail using X-ray diffraction, scanning electron microscopy, Fourier transform infrared, and UV-visible diffuse reflectance spectra techniques, and the excellent conditions for preparing spherical α-Fe$_2$O$_3$ nanoparticles with good dispersibility were obtained as follows: end pH was 8.9, ammonia concentration was 1.0 mol L^{-1}, precursor calcination temperature was 400°C. The optical bandgap energy (E_g) of the as-prepared α-Fe$_2$O$_3$ particles can be estimated by Tauc's equation to be 1.97 eV, and the strong and broad absorption in the visible light region (410–580 nm) presents its potential application as a visible light activate photocatalyst. In the presence of H$_2$O$_2$, the photocatalytic degradation rate of the as-prepared α-Fe$_2$O$_3$ nanoparticles to methyl orange (MO) and methylene blue (MB) is enhanced to 99% (150 min) and 97% (180 min), respectively, due to its role in forming more strong oxidizing •OH and inhibiting the recombination of electrons and holes.

Keywords: α-Fe$_2$O$_3$ nanoparticles; Photocatalytic degradation; Bandgap; Methyl orange dyes; Methylene blue dyes

1. Introduction

With the continuous development of modern industry, water pollution caused by organic dye molecules has become one of the serious environmental problems, which directly threatens human health and the survival of animals and plants [1–4].

Currently, semiconductor oxide photocatalytic degradation has become an effective approach to remove synthetic dyes [5–7]. Driven by visible light or ultraviolet light, holes, and electrons were formed on the surface of the catalyst, and produced strong oxidant, •OH to effectively decompose the dye into non-toxic carbon dioxide and other small molecules [8–10].

Considerable research efforts have been devoted to the preparation of TiO$_2$ photocatalysts and the improvement of their photocatalytic performance [11–13]. However, due to the relatively large bandgap (3.2 eV) of TiO$_2$, only ultraviolet light sources with a wavelength less than 385 nm can be used, which accounts for only about 5% of the total solar energy. Therefore, the development of photocatalysts with a smaller bandgap that can effectively use visible light energy has become a major research topic [14].

α-Fe$_2$O$_3$ is an n-type semiconductor material with many excellent properties of stable performance, natural

* Corresponding author.

abundance, low synthesis cost [15, 16], and environmentally friendly, especially its narrow bandgap of 2.0–2.2 eV makes it have strong visible light absorption performance, so it is considered to be a potential photocatalytic material [17–19]. Nevertheless, α-Fe$_2$O$_3$ as a photocatalyst has the disadvantage of high recombination rate and low hole diffusion length (2–4 nm) [20], which limits its photocatalytic activity is limited. Therefore, many efforts have been devoted to improving photocatalytic properties of the α-Fe$_2$O$_3$, including synthesizing α-Fe$_2$O$_3$ nanostructures with different shapes and sizes [21], doping different elements [22,23], noble metal loading and semiconductor compositing [24,25], preparing heterostructures [26], and so on.

In fact, it is an economic and effective route to enhance the photocatalytic performance of single-phase α-Fe$_2$O$_3$ by designing appropriate methods and controlling corresponding processes to obtain products with specific morphology and particle size, which can also avoid complex reaction conditions or use expensive materials. A simple solvothermal method has been used to prepare α-Fe$_2$O$_3$ microspheres and nanospheres respectively, where α-Fe$_2$O$_3$ nanospheres possess a larger surface and stronger light absorption [27]. Porous Fe$_2$O$_3$ nanorods can be synthesized using a surfactant-free chemical solution method combined with a subsequent annealing process, which exhibits high photocatalytic activities in the photodegradation of RhB and eosin B [28]. It is reported that grain-like α-Fe$_2$O$_3$ nanostructures can be obtained by a facile hydrothermal approach and used as the photocatalyst for the photocatalytic degradation of Congo red (CR) dyes [29]. Some scholars have also studied photocatalytic degradation of acetochlor by α-Fe$_2$O$_3$ nanoparticles with different morphologies (rotator nano α-Fe$_2$O$_3$, rice grains nano α-Fe$_2$O$_3$, hollow nano α-Fe$_2$O$_3$, eggshell nano α-Fe$_2$O$_3$, and spherical nano α-Fe$_2$O$_3$), and proved that hollow α-Fe$_2$O$_3$ nanoparticles have great potential as a catalyst to eliminate toxic organic pollutants in the environment [30]. Even though, a variety of α-Fe$_2$O$_3$ nanomaterials are developed and applied for the photocatalytic degradation of different dyes, but it is still necessary to develop simple and reliable methods to prepare uniform α-Fe$_2$O$_3$ nanostructures and to study the size- and shape-dependent photocatalytic properties [31].

In this study, we presented a simple and facile method of chemical precipitation-calcination to prepare spherical α-Fe$_2$O$_3$ nanoparticles. Herein, the photocatalytic behavior of the prepared α-Fe$_2$O$_3$ particles was evaluated by the photocatalytic degradation of two harmful organic dyes, methyl orange (MO) and methylene blue (MB) under visible light irradiation. The effects of solution pH, neutralizer concentration and calcination temperature on the structure, morphology, particle size, and degradation rate of α-Fe$_2$O$_3$ particles were investigated in detail. The main reactive species in the degradation process were proved by capture experiments.

2. Experimental

2.1. Preparation of α-Fe$_2$O$_3$

In a typical experiment, the iron-bearing precursor was synthesized by a co-precipitation method, followed by conducting a calcination process to prepare α-Fe$_2$O$_3$ particles as shown in Fig. 1. First, 0.1 mol L^{-1} hydrate ferric chloride (FeCl$_3$·6H$_2$O) solution and different concentrations of ammonia aqueous solution were configured as initial materials. Then 150 mL FeCl$_3$·6H$_2$O solution was poured into a three-necked flask heated by a water bath. As soon as the solution temperature reached 65°C, the mechanical agitation at the rate of 300 rpm was turned on, and a certain concentration of ammonia solution was dropped into the solution at the rate of 2 mL min^{-1}.

When the solution reached a predetermined pH, the addition of the aqueous ammonia solution was stopped, and the stirring reaction was maintained for 1 h. Then centrifugal separation was carried out to obtain the precursor precipitate which was washed three times with deionized water and dried thoroughly in a vacuum oven at 70°C. Finally, α-Fe$_2$O$_3$ particles were prepared by calcining the as-synthesized precursor at a preset temperature for 2 h in the muffle furnace at the heating rate of 5°C min^{-1}.

2.2. Sample characterization

Crystal structures of the prepared samples were identified by X-ray diffraction (XRD, Rigaku-Smartlab, Japan with Cu Kα radiation). Scanning electron microscopy (SEM, ZEISS-Sigma, Germany) were used to determine the micromorphology of prepared samples. Image J was used to calculate the particle diameters of the product. Fourier transformation infrared spectrometer (FT-IR, 8400S CE, SHIMADZU, Japan) was used to analyze the functional groups of prepared samples. A UV-vis spectrophotometer (TU-1901, Purkinje General, Beijing, China) with an integrating sphere was used to acquire the solid-state absorption and diffuse reflectance spectra (DRS) of the as-synthesized samples in the range of 350–750 nm. The effect of pH, ammonia concentration, and calcination temperature on the properties of the prepared α-Fe$_2$O$_3$ particles was characterized by its direct degradation to MO solution at a concentration of 20 mg L^{-1} for 1 h.

2.3. Photocatalytic property measurement

Photocatalytic properties of the prepared α-Fe$_2$O$_3$ nanoparticles were evaluated by measuring the photocatalytic degradation rate of MO and MB aqueous solutions. Photocatalytic experiments were conducted using a
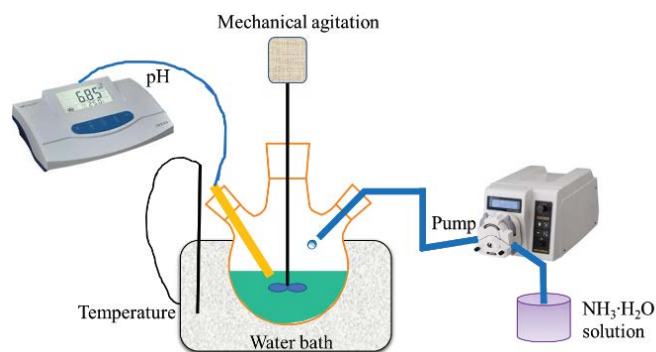

Fig. 1. Device chart for the synthesis of iron-containing precursor.

visible-light source of 150 W xenon lamp with a UV cutoff filter ($\lambda > 420$ nm). For each photocatalytic activity measurement, 0.2 g of as-prepared α-Fe$_2$O$_3$ particles were dispersed into 150 mL of MO (20 mg L^{-1}, pH = 3) and MB aqueous solution (5 mg L^{-1}, pH = 6.5), respectively. Prior to irradiation, the suspension was stirred in the dark at 25°C for a period of time to attain the adsorption–desorption equilibrium between the organic dye solution and α-Fe$_2$O$_3$. Then a certain amount (0.5 mL) of 30% hydrogen peroxide (H$_2$O$_2$) was added to the solution and reacted under ultraviolet-visible irradiation for 15~180 min with continuous stirring. At a regular interval (15 min), 4 mL of the suspensions were taken and centrifuged for measuring the concentrations of the MO or MB aqueous solutions by a UV-vis 1901 spectrophotometer at 504 nm or 664 nm, respectively.

3. Results and discussion

3.1. Effect of end pH value of the solution

The effect of the end pH value of reaction solution on the structure and properties of prepared α-Fe$_2$O$_3$ particles was studied by fixing other experimental conditions as follows: reaction temperature was 65°C, ammonia concentration was 1.0 mol L^{-1}, and the calcination temperature of the iron precursor was 400°C.

XRD patterns shown in Fig. 2 present that the pronounced diffraction peaks with 2θ = 24.1°, 33.1°, 35.6°, 40.8°, 49.4°, 54.0°, 62.4°, and 63.9° corresponded to the (012), (104), (110), (113), (024), (116), (214), and (300) crystal planes of α-Fe$_2$O$_3$, respectively. No diffraction peaks of other impurities are detected, indicating that the products are pure α-Fe$_2$O$_3$.

However, the α-Fe$_2$O$_3$ particles prepared by calcining iron-bearing precursors obtained under different pH have different crystallinity. By comparison, when the pH is 7, 8, and 8.3, the diffraction peak of the prepared α-Fe$_2$O$_3$ particles is sharp and the crystallinity is high. When the pH is 6, 8.6, and 8.9, the 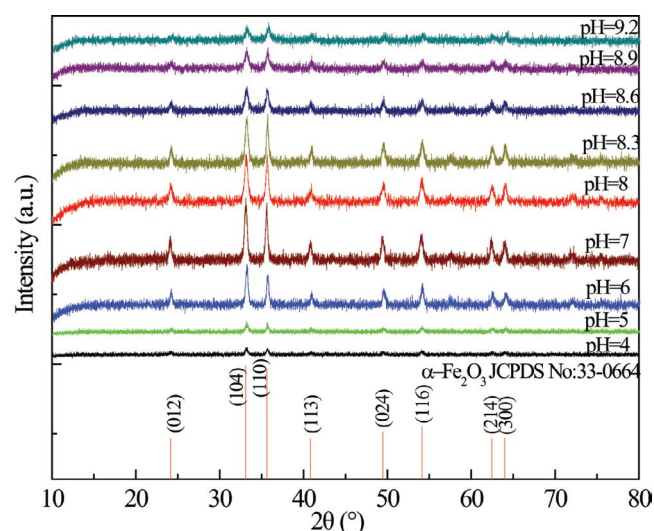intensity of the diffraction peak is slightly decreased, and the width of the half peak is increased, indicating that the crystallinity of the prepared α-Fe$_2$O$_3$ particles is lowered. When the pH is 4, 5, and 9.2, the intensity of the diffraction peak is weak, and the crystallinity of the prepared α-Fe$_2$O$_3$ particles is poor.

The photocatalytic activity of the prepared α-Fe$_2$O$_3$ particles is related to its crystallinity. When the particles have low crystallinity and many internal defects, it can capture photogenerated electrons, reducing the number of electrons involved in photodegradation, thereby decreasing photocatalytic efficiency. When the crystallinity of the particles is high, the internal lattice defects are few, which is beneficial to the conduction of charge carriers, but is not conducive to the separation of electron holes and recombination centers, so the activity of the catalyst is reduced. The α-Fe$_2$O$_3$ particles prepared from the reaction solutions with pH of 8.6, 8.9, and 9.2 have suitable crystallinity.

As seen in Fig. 3, the order of the solution pH value that caused the UV-visible absorbance curve to change from high to low is 4 > 5 > 6 > 7 > 8 > 8.3 > 9.2 > 8.6 > 8.9. When the solution pH value is ≤8, the degradation rate of MO by α-Fe$_2$O$_3$ is less than 15%, and the UV-visible absorption curve decreases slightly with the increase of pH value. When the solution pH value is ≥8.3, the UV-visible absorption curve is greatly decreased, and the degradation rate of MO by α-Fe$_2$O$_3$ is significantly increased, reaching a maximum of 55% at pH = 8.9. When the solution pH value is >8.9, the degradation rate of MO by α-Fe$_2$O$_3$ decreases with the increase of pH value.

The SEM images of α-Fe$_2$O$_3$ samples prepared by calcining the iron-bearing precursor obtained under different solution pH are shown in Fig. 4. It can be observed that the α-Fe$_2$O$_3$ particles are spherical-like in shape and their size has reached the nanometer level. The order of solution pH that caused the particle diameters to change from small to large is 9.2 < 8.6 < 8.3 < 8.9, and the degree of agglomeration of α-Fe$_2$O$_3$ particles from large to small is

Fig. 2. XRD patterns of α-Fe$_2$O$_3$ samples were prepared by calcining the precursor obtained under different solution pH values.
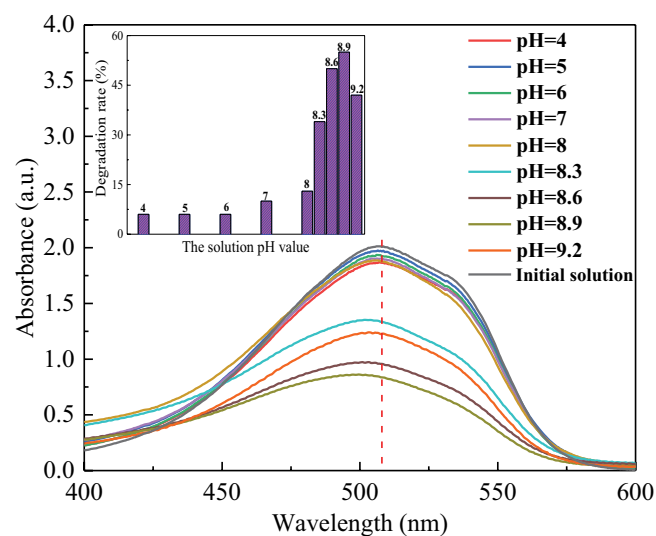

Fig. 3. UV-vis absorption spectra of degrading MO and the degradation rate of MO by α-Fe$_2$O$_3$ samples prepared by calcining the precursor obtained under different solution pH values.

9.2 > 8.6 > 8.3 > 8.9. When the solution pH value is 8.9, the prepared α-Fe$_2$O$_3$ particles have a relatively regular shape and good dispersibility.

The FT-IR spectrum of α-Fe$_2$O$_3$ particles in the frequency range of 500–4,000 cm^{-1} is shown in Fig. 5a. The absorption peaks at 3,421 and 1,650 cm^{-1} are caused by the stretching vibration and bending vibration of the O–H bond of the adsorbing water, respectively. The absorption peaks at 547 and 468 cm^{-1} correspond to the stretching vibration and bending vibration of the Fe–O bond, respectively, and the pH order affecting the intensity of the absorption peaks from small to large is 9.2 < 8.6 < 8.3 < 8.9.
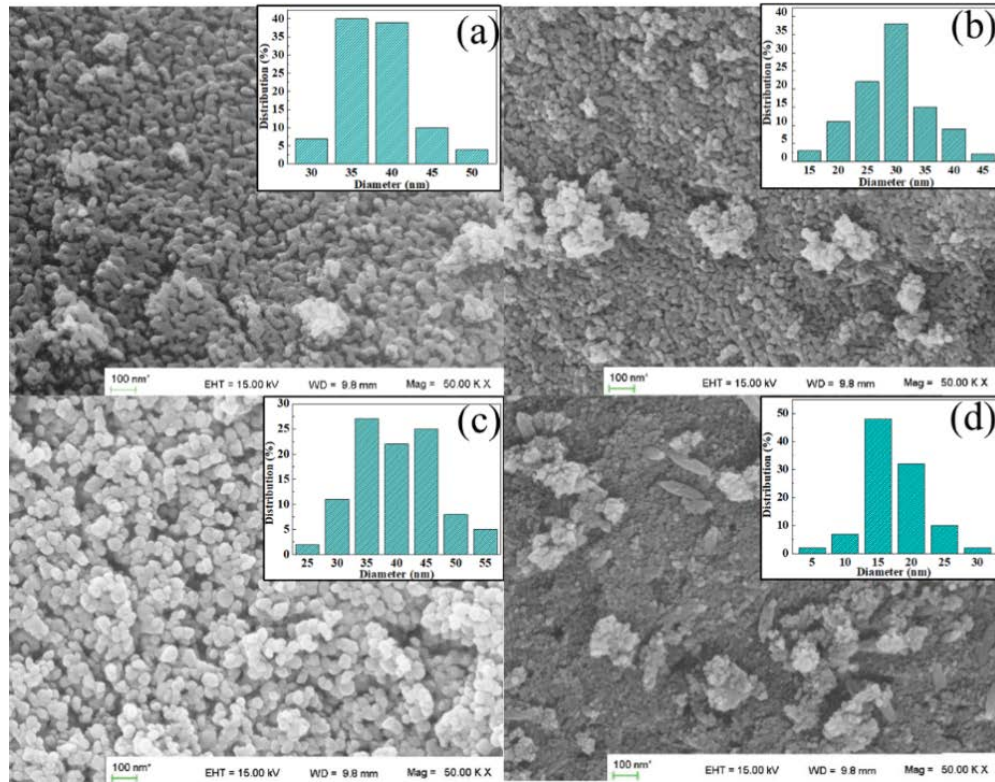

Fig. 4. SEM images of α-Fe$_2$O$_3$ samples prepared by calcining the precursor prepared under different solution pH values: (a) pH = 8.3, (b) pH = 8.6, (c) pH = 8.9, and (d) pH = 9.2.
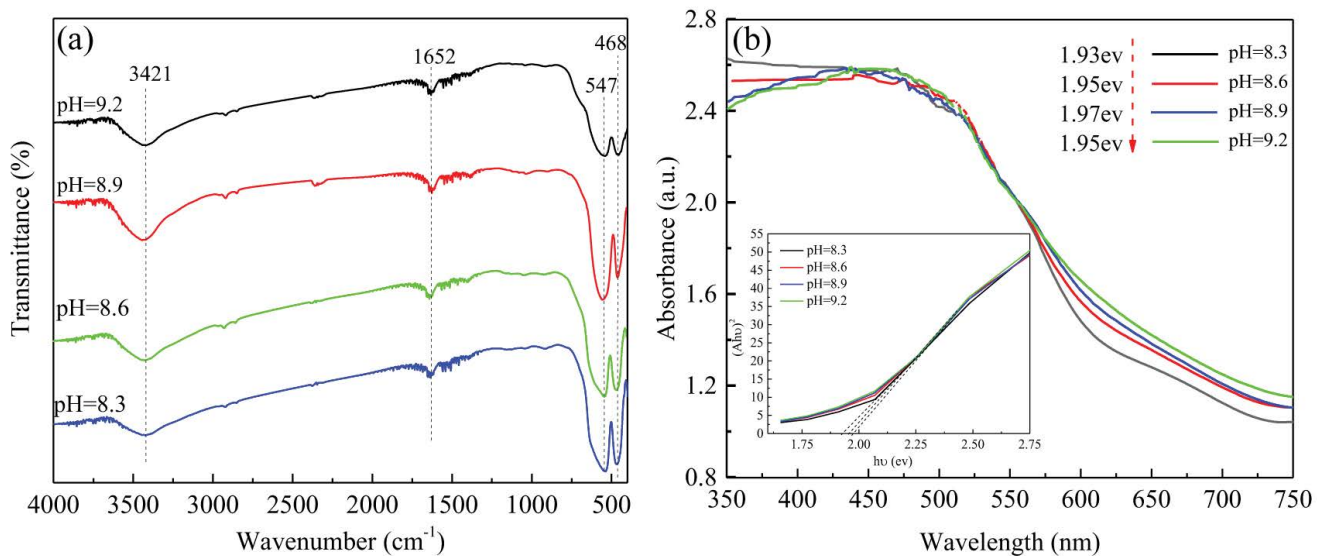

Fig. 5. (a) FT-IR spectra of the α-Fe$_2$O$_3$ samples and (b) UV-vis DRS and ($\alpha h\nu$)^2-$h\nu$ curves of the α-Fe$_2$O$_3$ samples.

The UV-vis DRS of α-Fe₂O₃ particles was used to determine its light absorbance property. The results in Fig. 5b show that the UV-visible diffuse reflection curves of α-Fe₂O₃ samples are similar in shape under different solution pH values. The prepared α-Fe₂O₃ samples have strong optical absorption in both ultraviolet light and visible light regions in the range of 350–750 nm. The absorption band edge of the sample is in the range of 600–650 nm, and the maximum absorption wavelength is ~470 nm, and the optical bandgap energy (E_g) of the α-Fe₂O₃ samples can be estimated by Tauc's equation as follows:

$$(\alpha h\nu)^{1/n} = A\left(h\nu - E_g\right) \tag{1}$$

where $h\nu$ is the photon energy, h is the Planck constant (6.63×10^{-34} J S), A is the band edge parameter constant, E_g is optical bandgap, and the exponent n is a constant that is determined by the type of optical transition. For direct allowed transition $n = 0.5$, and for indirect allowed transition $n = 2$. While α-Fe₂O₃ is an indirect inter-band transition, hence the value of n equals 0.5. The inset in Fig. 5b shows a Tauc plot of $(\alpha h\nu)^2$ vs. photon energy $h\nu$, and the bandgap energies of the α-Fe₂O₃ particles are estimated to be 1.93 eV (pH = 8.3), 1.95 eV (pH = 8.6), 1.97 eV (pH = 8.9), and 1.95 eV (pH = 9.2), respectively. The E_g values of α-Fe₂O₃ are similar to those reported by Liu et al. [8] and Li et al. [32], but are slightly smaller than those reported by Guo et al. [26] and Chen et al. [33]. When the solution pH is 8.9, the α-Fe₂O₃ has the largest E_g value, indicating that it has stronger electron reduction ability and hole oxidation ability, and less photogenerated electron–hole recombination probability, which is beneficial to photocatalysis. The results are consistent with the degradation rate of MO by the α-Fe₂O₃ samples in Fig. 3.

3.2. Effect of ammonia concentration

The effect of ammonia concentration used to precipitate iron-bearing precursors on the structure and properties of
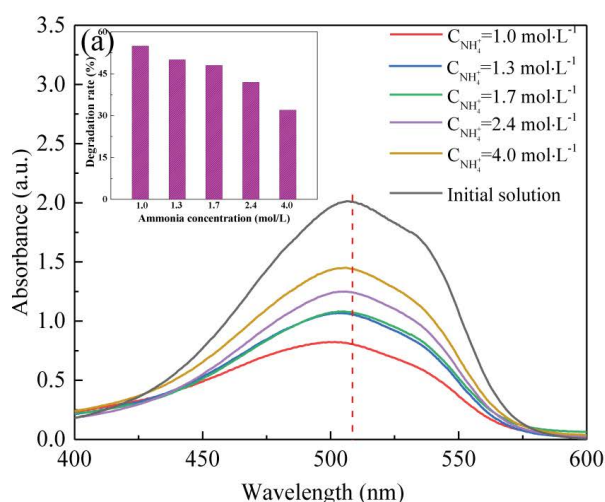
prepared α-Fe₂O₃ was studied when the reaction temperature was 65°C, the solution pH value was 8.9, and the calcination temperature of the iron-bearing precursor was 400°C.

All the diffraction peaks that appear at XRD patterns in Fig. 6 correspond to those crystal planes of α-Fe₂O₃, and no diffraction peaks of any other phases are detected, suggesting pure α-Fe₂O₃ is gained. When the ammonia concentration is 1.0 mol L⁻¹, the crystallinity of α-Fe₂O₃ obtained by calcination of the prepared iron-bearing precursor is relatively good.

Fig. 7a presents that with the decrease of ammonia concentration from 4.0 to 1.0 mol L⁻¹, the UV-visible absorption curve decreases significantly, and the degradation rate of MO by α-Fe₂O₃ is greatly increased to 55% when ammonia concentration is 1.0 mol L⁻¹. The reason is that when the ammonia concentration is low, the solution pH value increases slowly, which is beneficial
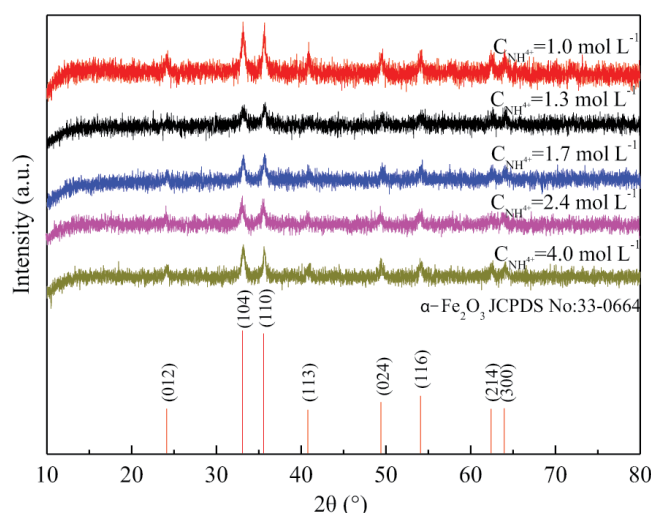

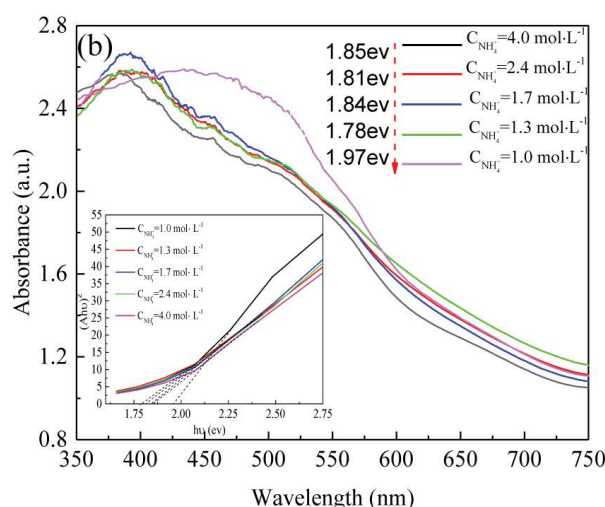Fig. 6. XRD patterns of α-Fe₂O₃ samples were prepared by calcining the precursor obtained under different ammonia concentrations.

Fig. 7. (a) UV-vis absorption spectra of degrading MO and the degradation rate of MO by α-Fe₂O₃ samples and (b) UV-vis DRS and $(\alpha h\nu)^2$-$h\nu$ curves of the α-Fe₂O₃ samples.

to the slow and uniform growth of the iron-bearing precursor, so that uniform-sized α-Fe$_2$O$_3$ can be prepared. The UV-visible DRS of α-Fe$_2$O$_3$ samples in Fig. 7b shows that the absorption band edge of the α-Fe$_2$O$_3$ sample is in the range of 620–650 nm, when ammonia concentration is 1.0 mol L^{-1}, and the bandgap energy (E_g) is the largest, which is not conducive to the recombination of photoexcited electrons and holes, thereby promoting the photocatalytic reactions on the sample surface. Moreover, the strong and broad absorption in the visible light region (410–580 nm) implies that α-Fe$_2$O$_3$ has the potential to be an efficient visible light activate photocatalyst.

Fig. 8 gives the SEM images and particle size distributions of α-Fe$_2$O$_3$ samples prepared by calcining the precursor obtained under different ammonia concentrations. It is indicated that α-Fe$_2$O$_3$ particles with different sizes are agglomerated together. With decreasing ammonia concentration from 4 to 1.3 mol L^{-1}, the particle sizes of the samples increase, and the dispersibility of the particles is also obviously improved. A plausible explanation is that the solution pH value increases due to the increase of ammonia concentration shorts the nucleation time of iron-bearing precursor, and causes the particle size of α-Fe$_2$O$_3$ samples to decrease. When ammonia concentration is 1.0 mol L^{-1}, the prepared α-Fe$_2$O$_3$ particles have a relatively regular shape and good dispersibility, as seen in Fig. 4c. In addition, the FT-IR spectrum of α-Fe$_2$O$_3$ in Fig. 9 exhibits the stronger absorption peaks of Fe–O bond at 547 and 468 cm^{-1}, respectively, illustrating the formation of α-Fe$_2$O$_3$. Meanwhile, the stronger absorption peaks of the O–H bond at 3,421 and 1,650 cm^{-1}, respectively, indicate that the product has a larger specific surface area so that it can absorb more water.

3.3. Effect of the calcination temperature of the precursor

The iron-bearing precursor was calcined at 400°C, 450°C, 500°C, and 550°C, respectively, to investigate the effect of calcination temperature on the structure and properties of prepared α-Fe$_2$O$_3$ samples. The XRD patterns in Fig. 10 present that the calcination temperature has little effect on the crystallinity and phase of formed α-Fe$_2$O$_3$. However, the micromorphology and crystal size are affected significantly by calcination temperature. From the SEM images in Fig. 10b–d, it can be seen that the
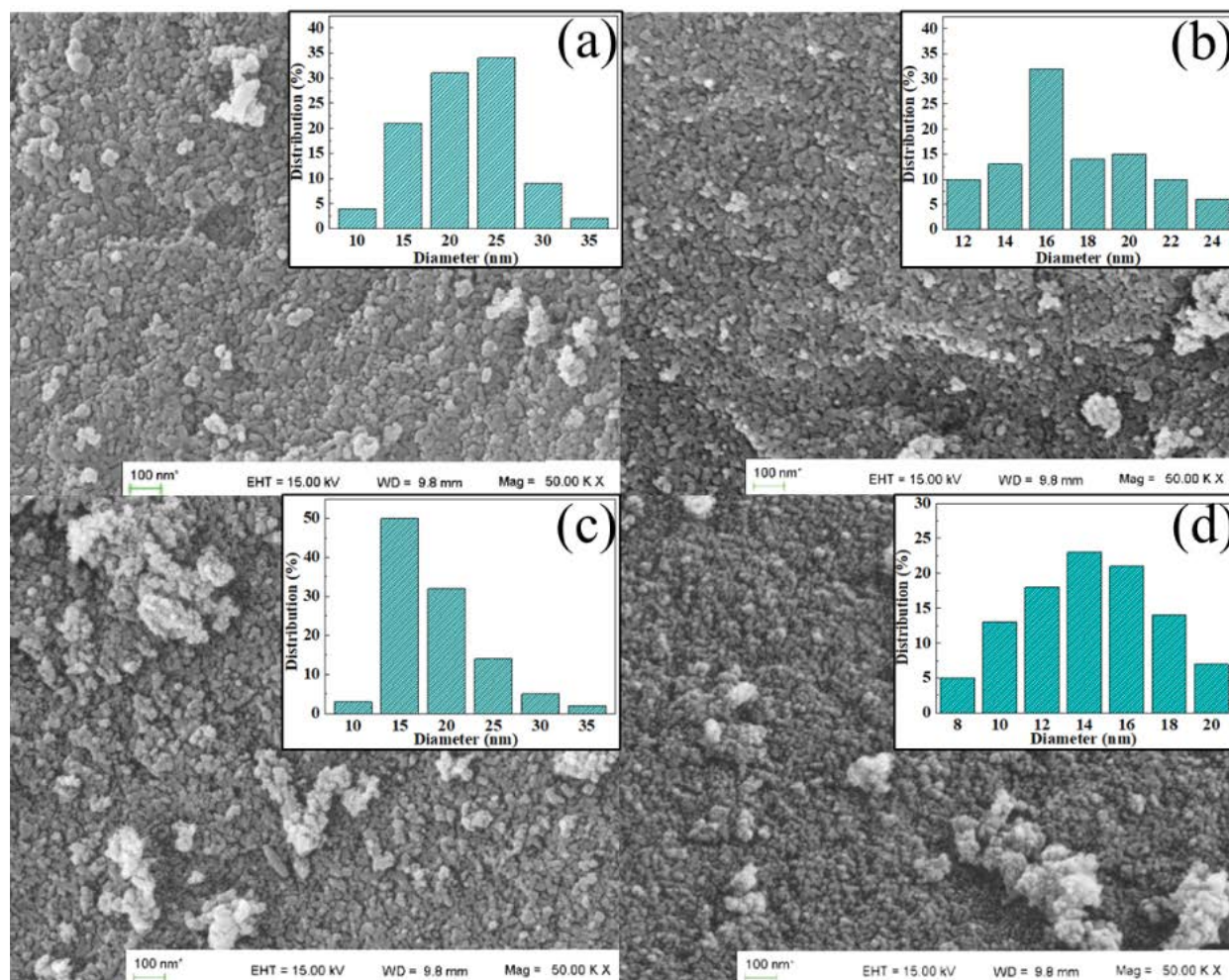

Fig. 8. SEM micromorphology of α-Fe$_2$O$_3$ prepared by calcining the precursor obtained under different ammonia concentrations: (a) 1.3 mol L^{-1}, (b) 1.7 mol L^{-1}, (c) 2.4 mol L^{-1}, and (d) 4 mol L^{-1}.

prepared α-Fe₂O₃ is spherical-like granular when the calcination temperature varies in the range of 450°C–550°C. Compared with Fig. 4c, the α-Fe₂O₃ microparticle size is reduced and mainly distributes in the range of 15–35 nm. Agglomeration occurs in all samples, and the degree increases with increasing temperature, which results in a decrease in the specific surface area of the particles, a decline of the adsorption performance, and ultimately the reduction of the degradation rate of α-Fe₂O₃. Although the particle size of α-Fe₂O₃ obtained at 400°C is slightly increased, the morphology is more uniform and dispersed.

From FT-IR spectrum of the samples in Fig. 11, it can be seen that the stronger absorption peaks of Fe–O bond at 547 and 468 cm⁻¹, respectively, have proved the successful
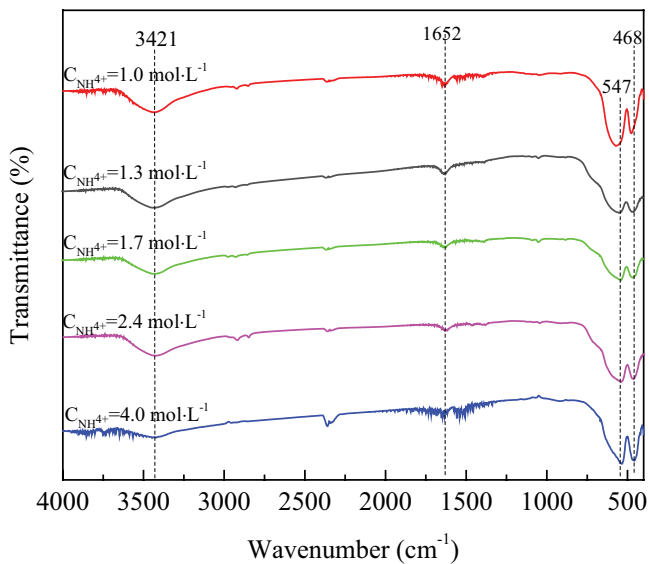
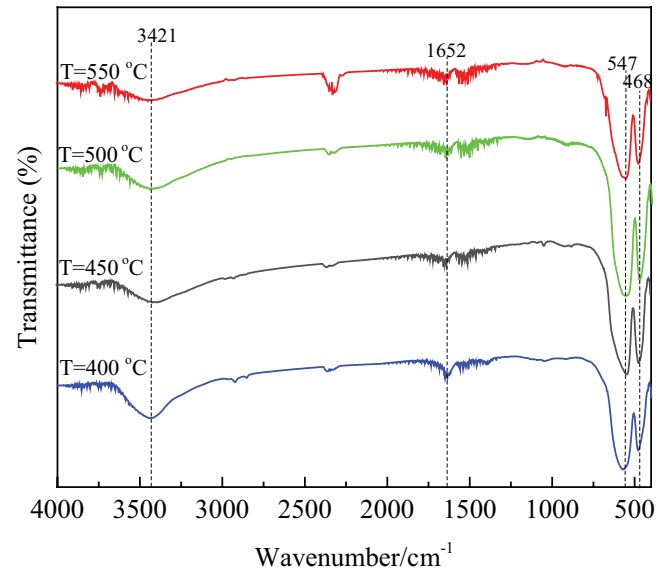Fig. 9. FT-IR spectra of α-Fe₂O₃ prepared by calcining the precursor obtained under different ammonia concentrations.

Fig. 11. FT-IR spectra of α-Fe₂O₃ prepared by calcining the precursor under different temperatures.

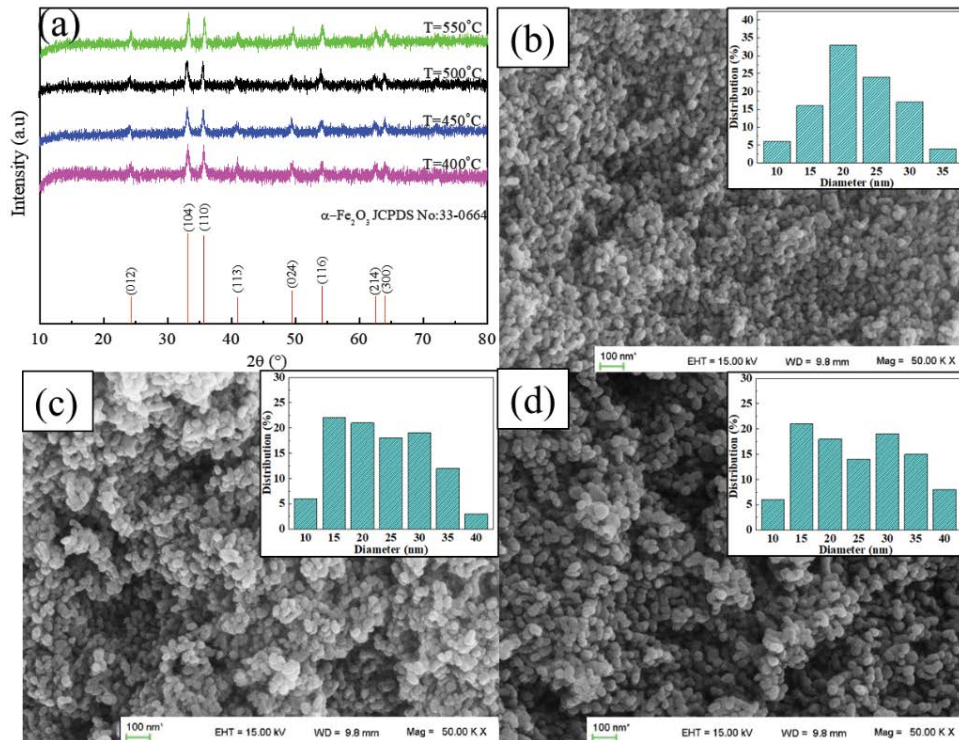Fig. 10. (a) XRD patterns of α-Fe₂O₃, and SEM images of α-Fe₂O₃ prepared by calcining the precursor under different temperatures, (b) 450°C, (c) 500°C, and (d) 550°C.

formation of α-Fe$_2$O$_3$. The –OH bond of the sample prepared at 400°C has a broader and deeper absorption peak at 3,421 and 1,650 cm^{-1}, respectively, which is caused by the larger specific surface area of the sample particles and the more water adsorbed on the surface.

The UV-visible absorption curves and degradation rate of α-Fe$_2$O$_3$ samples obtained at different calcination temperatures for MO solution are shown in Fig. 12a. The results presented that as the calcination temperature increases, the reduction extent of UV-visible absorption curves increases. When the calcination temperature is 400°C, the greatest degradation rate of 55% is reached.

The UV-visible DRS of α-Fe$_2$O$_3$ samples in Fig. 12b shows that the absorption band edge of the α-Fe$_2$O$_3$ sample is in the range of 600–650 nm. When the calcination temperature is 400°C, the absorption intensity of the sample for UV light (350–415 nm) is the smallest, but the absorption intensity for visible light (415–675 nm) is greatly increased, which results in an increase in the photocatalytic activity of the sample. Meanwhile, the absorption band edges of the α-Fe$_2$O$_3$ samples prepared at a temperature higher than 400°C blue-shifts significantly in the visible light range (415–675 nm), thus the photocatalytic activity of α-Fe$_2$O$_3$ samples is decreased. In addition, with the increase of calcination temperature, the bandgap energy (E_g) of α-Fe$_2$O$_3$ samples decreases, which increases the probability of recombination of electrons and holes.

3.4. Photocatalytic degradation of MO and MB dyes

The photocatalytic degradation results of the prepared α-Fe$_2$O$_3$ samples for MO and MB solutions are shown in Figs. 13a–d and 14a–d, respectively. The degradation process of organic dyes is divided into two stages: adsorption–desorption stage (A) and photocatalytic degradation reaction stage (P).

It can be seen from Fig. 13a that the adsorption equilibrium between α-Fe$_2$O$_3$ samples and MO solution is reached within A-20 min of the dark reaction without light, and the adsorption rate is 56%. The absorbance of the MO solution increases when the degradation reaction is P-15 min (Fig. 13b and c), regardless of whether the source is irradiated or not. This can be attributed to the addition of H$_2$O$_2$, which destroys the formed adsorption–desorption equilibrium, resulting in partial desorption of MO molecules adsorbs on the surface of α-Fe$_2$O$_3$ samples.

In the absence of no light irradiation, the absorbance of the MO solution slowly decreases with the increase of time (Fig. 13c). When the time is 20 min, the absorbance reaches the lowest point, which shows that the adsorption equilibrium is reached, and the degradation rate of MO increases gradually and reaches 75% at P-180 min (Fig. 13d), which illustrates that H$_2$O$_2$ can decompose a part of MO molecules.

When the degradation is carried out under light irradiation, the absorbance of the MO solution decreases significantly with time. When the time is ≥P-60 min, the absorbance curve is close to the horizontal line (Fig. 13b and c), and the degradation rate of MO is over 90%. After that, with the increase of time, the degradation rate of the MO solution decreases slowly and reaches more than 99% at P-150 min (Fig. 13d).

Compared with the photocatalytic degradation without H$_2$O$_2$, the degradation rate is increased by approximately 40%, while compared with that without light irradiation, the degradation rate is increased by approximately 25%. These results indicate that the addition of H$_2$O$_2$ can not only significantly shorten the photocatalytic time, but also improve the photocatalytic degradation rate.

Fig. 14a presents that the adsorption rate of α-Fe$_2$O$_3$ samples to MB solution is only approximately 4% within A-20 min of the dark reaction without light, which is much lower than that of MO. When H$_2$O$_2$ is added, the adsorption–desorption equilibrium of α-Fe$_2$O$_3$ samples to MB solution is not affected.

When no light irradiates, the absorbance of MB solution decreases slightly with the increase of time (Fig. 14a and c), and the degradation rate of MB only reaches approximately 10% at P-180 min (Fig. 14d), which indicates that the decomposition of MB by H$_2$O$_2$ is weaker than that of MO.
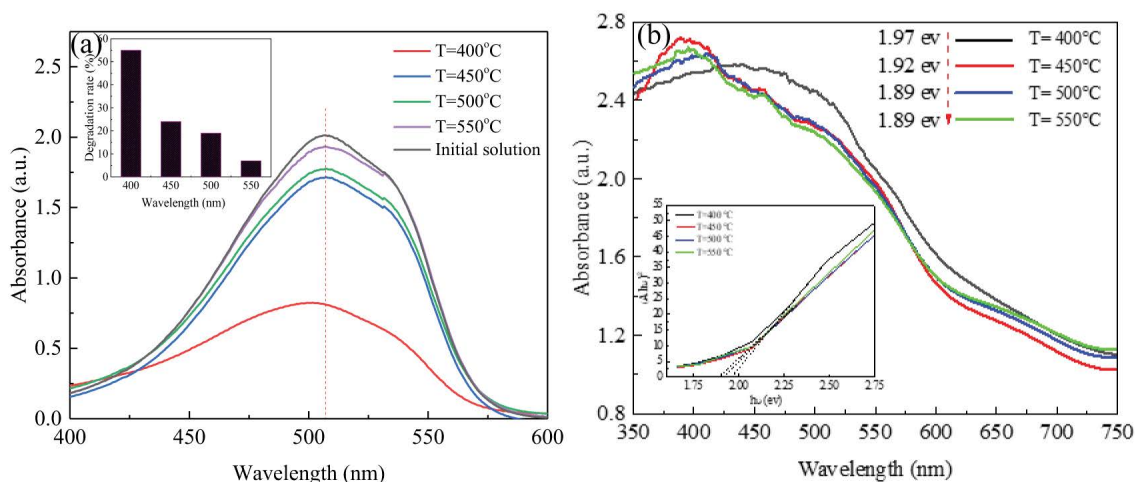

Fig. 12. (a) UV-vis absorption spectra of degrading MO and the degradation rate of MO by α-Fe$_2$O$_3$ and (b) UV-vis DRS and $(\alpha h\nu)^2$-$h\nu$ curves of the α-Fe$_2$O$_3$ samples.
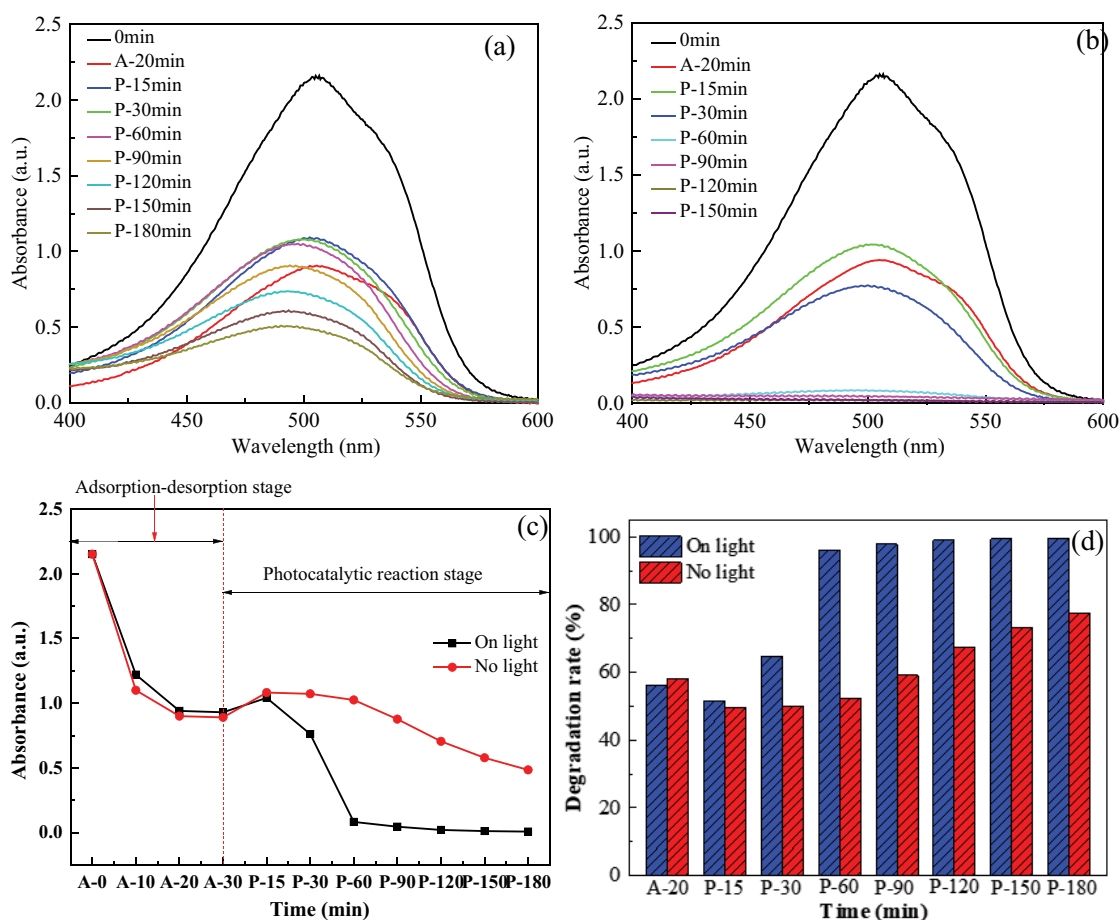
Fig. 13. UV-vis absorption spectra of α-Fe$_2$O$_3$ for the degradation of MO solution: (a) no light and (b) on light; (c) the absorbance and (d) the degradation rate of MO by α-Fe$_2$O$_3$ varied with time.

When exposed to light, the absorbance of MB solution decreases significantly with the increase of photocatalytic degradation time, and the degradation rate of MB also increases rapidly. At the time of P-180 min, almost complete degradation of MB (≥97%) is achieved. The results show that the prepared α-Fe$_2$O$_3$ samples also have excellent photocatalytic degradation properties for MB dyes in the presence of H$_2$O$_2$.

Under the ultraviolet or visible light irradiation, photogenerated electrons in the α-Fe$_2$O$_3$ crystal are excited from valence band (VB) to conduction band (CB), and holes are formed in VB (Eq. (2)). A lot of electrons and holes migrate to the surface of α-Fe$_2$O$_3$, and they also have the possibility of recombination. The dissolved O$_2$ adsorbed on the surface of α-Fe$_2$O$_3$ can capture electrons to produce the oxygen free radicals (•O$_2^-$) according to Eq. (3), and the hydroxide ions and water adsorbed on the surface of α-Fe$_2$O$_3$ can be oxidized by the holes to form hydroxyl radicals (•OH) with high oxidation and reactivity according to Eqs. (4) and (5). As the powerful oxidant, •O$_2^-$ and OH can decompose effectively the organic dyes such as MB and MO to generate non-toxic gases such as carbon dioxide and water, as shown in Eq. (7). When H$_2$O$_2$ is present in the reaction system, it can combine with electrons to form more •OH according to Eq. (6), inhibiting the recombination of electrons and

holes, thereby improving the degradation rate of the dyes and the photocatalytic properties. The schematic diagram of photocatalytic degradation of MB or MO by α-Fe$_2$O$_3$ nanoparticles is shown in Fig. 15a.

In order to detect the active substances in the photocatalytic reaction, *tert*-butanol (TBA), benzoquinone (BQ), and EDTA-2Na are used to capture hydroxyl radicals (•OH), oxygen-free radicals (•O$_2^-$), and holes (h$^+$). The results shown in Fig. 15b present that the addition of EDTA-2Na and BQ significantly reduces the photocatalytic degradation rate; while the addition of TBA has little effect on the photocatalytic degradation rate. Therefore, •OH and h+ are the main reactive species in the photocatalytic degradation of α-Fe$_2$O$_3$.

$$\alpha - Fe_2O_3 + h\nu \rightarrow h_{VB}^+ + e_{CB}^- \tag{2}$$

$$e_{CB}^- + O_2 \rightarrow {}^{\bullet}O_2^- \tag{3}$$

$$h_{VB}^+ + OH^- \rightarrow {}^{\bullet}OH \tag{4}$$
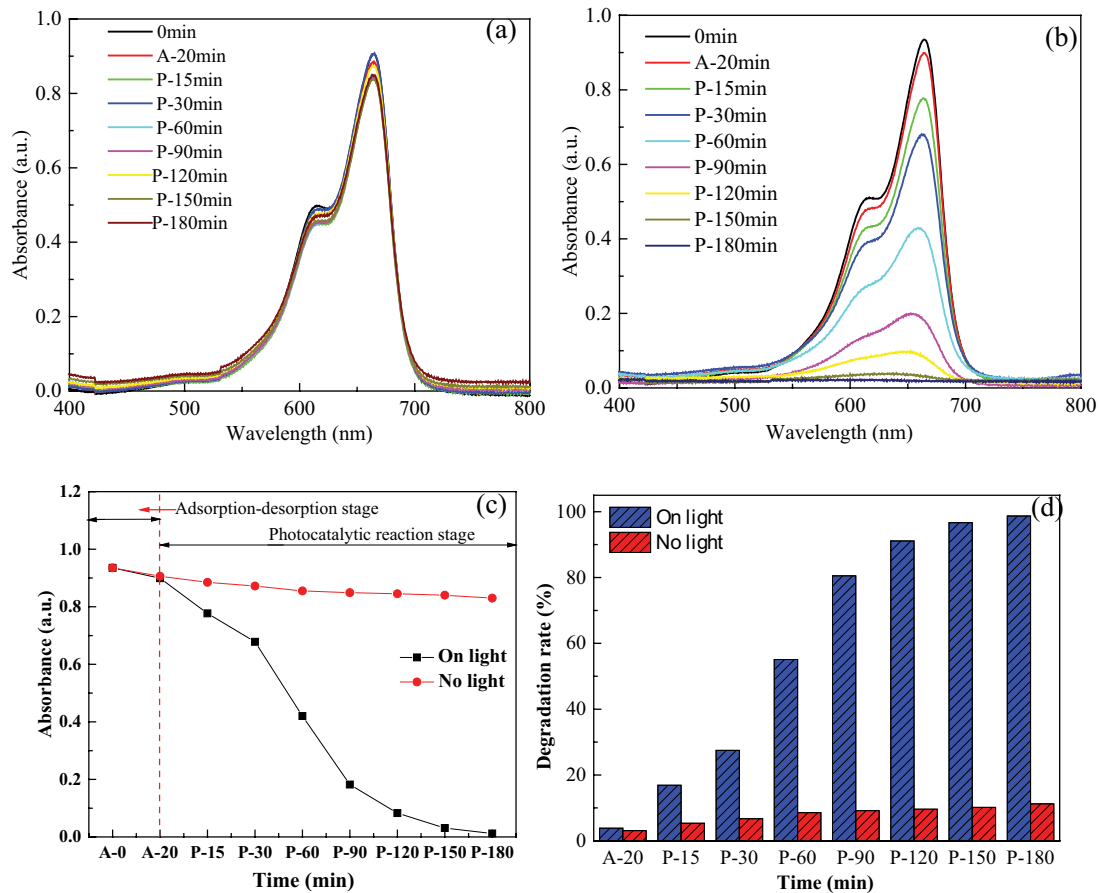
$$h_{VB}^+ + H_2O \rightarrow {}^{\bullet}OH + H^+ \tag{5}$$

Fig. 14. UV-vis absorption spectra of α-Fe$_2$O$_3$ for degradation of MB solution: (a) no light and (b) on light; (c) the absorbance and (d) the degradation rate of MB by α-Fe$_2$O$_3$ varied with time.
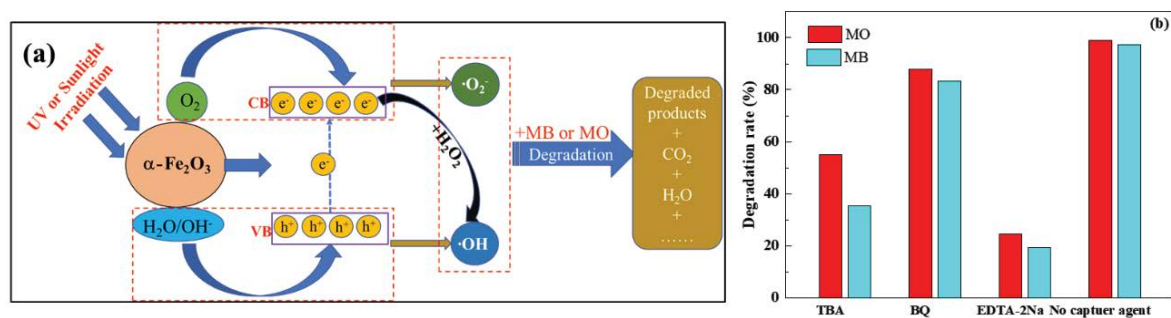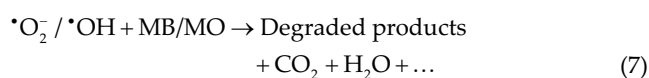

Fig. 15. Photocatalytic degradation of MB or MO by α-Fe$_2$O$_3$ nanoparticles: (a) schematic diagram of degradation and (b) capturing experimental results.

$$e_{CB}^{-} + H_2O_2 \rightarrow {}^{\bullet}OH + OH^{-} \tag{6}$$

$$
\begin{aligned}
{}^{\bullet}O_2^{-} / {}^{\bullet}OH + MB/MO &\rightarrow \text{Degraded products} \\
&+ CO_2 + H_2O + \dots
\end{aligned}
\tag{7}
$$

4. Conclusions

A α-Fe$_2$O$_3$ nano photocatalyst was successfully prepared via a simple process of chemical precipitation-calcination

and characterized using XRD, SEM, FT-IR, and UV-visible DRS techniques. The effects of solution end pH, ammonia concentration, and precursor calcination temperature on the morphology, structure, and properties of the prepared products were studied in detail, and the excellent conditions for preparing spherical α-Fe$_2$O$_3$ nanoparticles with good dispersibility are as follows: pH is 8.9, ammonia concentration is 1.0 mol L^{-1}, the precursor calcination temperature is 400°C. The optical bandgap energy (E_g) of the prepared α-Fe$_2$O$_3$ nanoparticles is estimated by Tauc's equation to be 1.97 eV, and the strong and broad absorption in the visible

light region (410–580 nm) presents its potential application as a visible light activate photocatalyst.

By studying the adsorption, non-light oxidation, and photocatalytic degradation of MO and MB solution by α-Fe_2O_3 nanoparticles, it is found that the adsorption performance of α-Fe_2O_3 on MO (56%) is better than that of MB (4%), and H_2O_2 is also more susceptible to oxidize MO under no light irradiation. Strong oxidizing $^\bullet O_2^-$ and $^\bullet OH$ play important roles in the photocatalytic process. In the presence of H_2O_2, the photocatalytic degradation rates of the as-prepared α-Fe_2O_3 nanoparticles to MO and MB are enhanced to 99% (150 min) and 97% (180 min), respectively, due to its role in forming more strong oxidizing $^\bullet OH$ and inhibiting the recombination of electrons and holes. The main reactive species in the photocatalytic degradation of α-Fe_2O_3 are $^\bullet OH$ and h^+.

Acknowledgments

References

[1] L. Liu, J. Zhang, Y. Tan, Y. Jiang, M. Hu, S. Li, Q. Zhai, Rapid decolorization of anthraquinone and triphenyl-methane dye using chloroperoxidase: catalytic mechanism, analysis of products and degradation route, Chem. Eng. J., 244 (2014) 9–18.

[2] V. Katheresan, J. Kansedo, S.Y. Lau, Efficiency of various recent wastewater dye removal methods: a review, J. Environ. Chem. Eng., 6 (2018) 4676–4697.

[3] E.A. Abdelrahman, R.M. Hegazey, Y.H. Kotp, A. Alharbi, Facile synthesis of Fe_2O_3 nanoparticles from Egyptian insecticide cans for efficient photocatalytic degradation of methylene blue and crystal violet dyes, Spectrochim. Acta, Part A, 222 (2019) 117195–117206.

[4] M.A.M. Al-Alwani, N.A. Ludin, A. Bakar, A. Amir, H. Kadhum, A. Mukhlus, Application of dyes extracted from *Alternanthera dentata* leaves and *Musa acuminata* bracts as natural sensitizers for dye-sensitized solar cells, Spectrochim. Acta, Part A, 192 (2018) 487–498.

[5] M.R. Hoffmann, S.T. Martin, W. Choi, D.W. Bahnemann, Environmental applications of semiconductor photocatalysis, Chem. Rev., 95 (1995) 69–96.

[6] Y. Zhou, F. Krumeich, A. Heel, G.R. Patzke, One-step hydrothermal coating approach to photocatalytically active oxide composites, Dalton Trans., 39 (2010) 6043–6048.

[7] X. Li, B. Jin, J. Huang, Q. Zhang, R. Peng, S. Chu, Fe_2O_3/ZnO/$ZnFe_2O_4$ composites for the efficient photocatalytic degradation of organic dyes under visible light, Solid State Sci., 80 (2018) 6–14.

[8] J. Liu, B. Wang, Z. Li, Z. Wu, K. Zhu, J. Zhuang, Q. Xi, Y. Hou, J. Chen, M. Cong, J. Li, G. Qian, Z. Lin, Photo-Fenton reaction and H_2O_2 enhanced photocatalytic activity of α-Fe_2O_3 nanoparticles obtained by a simple decomposition route, J. Alloys Compd., 771 (2019) 398–405.

[9] D. Deng, K.S. Novoselov, Q. Fu, N. Zheng, Z. Tian, X. Bao, Catalysis with two-dimensional materials and their heterostructures, Nat. Nanotechnol., 11 (2016) 218–230.

[10] B. Feng, Z. Wu, J. Liu, K. Zhu, Z. Li, X. Jin, Y. Hou, Q. Xi, M. Cong, P. Liu, Q.L. Gu, Combination of ultrafast dye-sensitized-assisted electron transfer process and novel Z-scheme

[11] system: AgBr nanoparticles interspersed MoO_3 nanobelts for enhancing photocatalytic performance of RhB, Appl. Catal., B, 206 (2017) 242–251.

[11] M.M. Khan, S.A. Ansari, D. Pradhan, M.O. Ansari, D.H. Han, J. Lee, M.H. Cho, Band gap engineered TiO_2 nanoparticles for visible light induced photoelectrochemical and photocatalytic studies, J. Mater. Chem. A, 2 (2014) 637–644.

[12] M.M. Khan, J. Lee, M.H. Cho, Au@TiO_2 nanocomposites for the catalytic degradation of methyl orange and methylene blue: an electron relay effect, J. Ind. Eng. Chem., 20 (2014) 1584–1590.

[13] S. Hoang, S. Guo, N.T. Hahn, A.J. Bard, C.B. Mullins, Visible light driven photoelectrochemical water oxidation on nitrogen-modified TiO_2 nanowires, Nano Lett., 12 (2011) 26–32.

[14] L. Zhang, Y. Zhu, A review of controllable synthesis and enhancement of performances of bismuth tungstate visible-light-driven photocatalysts, Catal. Sci. Technol., 2 (2012) 694–706.

[15] J. Zhu, Z. Yin, D. Yang, T. Sun, H. Yu, H.E. Hoster, H.H. Hng, H. Zhang, Q. Yan, Hierarchical hollow spheres composed of ultrathin Fe_2O_3 nanosheets for lithium storage and photocatalytic water oxidation, Energy Environ. Sci., 6 (2013) 987–993.

[16] E. Alp, H. Eşgin, M.K. Kazmanlı, A. Genç, Synergetic activity enhancement in 2D CuO-Fe_2O_3 nanocomposites for the photodegradation of rhodamine B, Ceram. Int., 4 (2019) 9174–9178.

[17] J. Fang, J. Xu, J. Chen, X. Huang, W. Xun, Enhanced photocatalytic activity of molecular imprinted nano α-Fe_2O_3 by hydrothermal synthesis using methylene blue as structure-directing agent, Colloids Surf., A, 508 (2016) 124–134.

[18] H. Liang, K. Liu, Y. Ni, Synthesis of mesoporous α-Fe_2O_3 via sol–gel methods using cellulose nano-crystals (CNC) as template and its photo-catalytic properties, Mater. Lett., 159 (2015) 218–220.

[19] A. Kusior, K. Michalec, P. Jelen, M. Radecka, Shaped Fe_2O_3 nanoparticles-synthesis and enhanced photocatalytic degradation towards RhB, Appl. Surf. Sci., 476 (2019) 342–352.

[20] M. Mishra, H. Park, D.M. Chun, Photocatalytic properties of Au/Fe_2O_3 nano-composites prepared by co-precipitation, Adv. Powder Technol., 27 (2016) 130–138.

[21] S. Bharathi, D. Nataraj, K. Senthil, Y. Masuda, Shape-controlled synthesis of α-Fe_2O_3 nanostructures: engineering their surface properties for improved photocatalytic degradation efficiency, Nanotechnol. Sustainable Dev., 15 (2014) 113–125.

[22] G.K. Pradhan, S. Martha, K.M. Parida, Synthesis of multifunctional nanostructured zinc–iron mixed oxide photocatalyst by a simple solution-combustion technique, ACS Appl. Mater. Interfaces, 4 (2012) 707–713.

[23] C. Miao, T. Shi, G. Xu, S. Ji, C. Ye, Photocurrent enhancement for Ti-doped Fe_2O_3 thin film photoanodes by an in situ solid-state reaction method, ACS Appl. Mater. Interfaces, 5 (2013) 1310–1316.

[24] Y. Cong, Y. Ge, T. Zhang, Q. Wang, M. Shao, Y. Zhang, Fabrication of Z-scheme Fe_2O_3-MoS_2-Cu_2O ternary nanofilm with significantly enhanced photoelectrocatalytic performance, Ind. Eng. Chem. Res., 420 (2017) 669–680.

[25] Y.G. Xu, S.Q. Huang, M. Xie, Y.P. Li, H. Xu, L.Y. Huang, Q. Zhang, H.M. Li, Magnetically separable Fe_2O_3/g-C_3N_4 catalyst with enhanced photocatalytic activity, RSC Adv., 5 (2015) 95727–95735.

[26] R. Guo, X. Qi, X. Zhang, H. Zhang, X. Cheng, Synthesis of Ag_2CO_3/α-Fe_2O_3 heterojunction and it high visible light driven photocatalytic activity for elimination of organic pollutants, Sep. Purif. Technol., 211 (2019) 504–513.

[27] W. Chao, Z. Huang, Controlled synthesis of α-Fe_2O_3 nanostructures for efficient photocatalysis, Mater. Lett., 164 (2016) 194–197.

[28] X. Liu, K. Chen, J. Shim, J. Huang, Facile synthesis of porous Fe_2O_3 nanorods and their photocatalytic properties, J. Saudi Chem. Soc., 19 (2015) 479–484.

[29] Y. Dong, L. Xing, F. Hu, A. Umar, X. Wu, Efficient removal of organic dyes molecules by grain-like α-Fe_2O_3 nanostructures under visible light irradiation, Vacuum, 150 (2018) 35–40.

[30] Y. Fu, Y. Li, J. Hu, S. Li, G. Qin, Photocatalytic degradation of acetochlor by α-Fe$_2$O$_3$ nanoparticles with different morphologies in aqueous solution system, Optik, 178 (2019) 36–44.

[31] Y. Jiao, Y. Liu, F. Qu, A. Umar, X. Wu, Visible-light-driven photocatalytic properties of simply synthesized a-Iron(III)oxide nanourchins, J. Colloid Interface Sci., 451 (2015) 93–100.

[32] Y. Li, Y. Cao, D. Jia, Y. Wang, J. Xie, Solid-state chemical synthesis of mesoporous α-Fe$_2$O$_3$ nanostructures with enhanced xylene-sensing properties, Sens. Actuators, B, 198 (2014) 360–365.

[33] R. Chen, C. Zhu, J. Lu, J. Xiao, Y. Lei, Z. Yu, BiVO$_4$/α-Fe$_2$O$_3$ catalytic degradation of gaseous benzene: preparation, characterization and photocatalytic properties, Appl. Surf. Sci., 427 (2018) 141–147.